Chemical Science

ROYAL SOCIETY OF CHEMISTRY

EDGE ARTICLE

View Article Online
View Journal | View Issue

Cite this: *Chem. Sci.*, 2022, **13**, 11320

All publication charges for this article have been paid for by the Royal Society of Chemistry

Received 25th July 2022
Accepted 26th August 2022

DOI: 10.1039/d2sc04143j

rsc.li/chemical-science

Non-flammable, dilute, and hydrous organic electrolytes for reversible Zn batteries†

Guoqiang Ma,‡[a] Licheng Miao,‡[c] Wentao Yuan,[a] Kaiyue Qiu,[a] Mengyu Liu,[a] Xueyu Nie,[a] Yang Dong,[b] Ning Zhang *[a] and Fangyi Cheng *[bd]

Rechargeable Zn batteries hold great practicability for cost-effective sustainable energy storage but suffer from irreversibility of the Zn anode in aqueous electrolytes due to parasitic H_2 evolution, corrosion, and dendrite growth. Herein, we report a non-flammable, dilute, and hydrous organic electrolyte by dissolving low-cost hydrated $Zn(ClO_4)_2 \cdot 6H_2O$ in trimethyl phosphate (TMP), which homogenizes plating/stripping and enables *in situ* formation of a $Zn_3(PO_4)_2$–$ZnCl_2$-rich interphase to stabilize the Zn anode. A dilute 0.5 m $Zn(ClO_4)_2 \cdot 6H_2O$/TMP electrolyte featuring a H_2O-poor Zn^{2+}-solvation sheath and low water activity enables significantly enhanced Zn reversibility and a wider electrochemical window than the concentrated counterpart. In this formulated electrolyte, the Zn anode exhibits a high efficiency of 99.5% over 500 cycles, long-term cycling for 1200 h (5 mA h cm^{-2} at 5 mA cm^{-2}) and stable operation at 50 °C. The results would guide the design of hydrous organic electrolytes for practical rechargeable batteries employing metallic electrode materials.

Introduction

Rechargeable Zn batteries (RZBs) are promising candidates for large-scale energy storage applications, benefiting from the advantages of Zn such as an abundant reservoir, low cost, and high theoretical specific gravimetric/volumetric capacity (820 mA h g^{-1} and 5855 mA h cm^{-3}). Most RZBs employ aqueous electrolytes that feature high safety and good environmental compatibility.[1–4] Nonetheless, in aqueous electrolytes, Zn metal anodes are generally plagued by severe irreversibility caused by water-induced side reactions (*e.g.*, H_2 evolution and Zn corrosion).[5–8] In non-aqueous Li batteries, the formation of a stable solid electrolyte interphase (SEI) derived from the decomposition of an organic solvent and/or salt anion allows ionic transport but blocks the solvents and electrons, which is critical for the reversible cycling of metal anodes.[9–11] Unfortunately, the water decomposition along with H_2 evolution in aqueous electrolytes makes it difficult to form a protective SEI on Zn anodes. Instead, the elevation of local pH near the Zn surface incurs the formation of loose by-products of hydroxides/oxides, causing low Zn plating/stripping efficiency.[12–15] Simultaneously, the rampant dendritic Zn growth in aqueous electrolytes would exacerbate the parasitic reactions and battery failure.[16–18]

Effective strategies to stabilize Zn anodes include designing highly concentrated aqueous electrolytes[19–23] and using aqueous–organic hybrid electrolytes.[24–29] Alternatively, exploring organic electrolytes would offer another opportunity to boost Zn reversibility because of the high thermodynamic stability of Zn in organic solvents.[30–33] However, nonaqueous RZBs often employ solvents of acetonitrile (AN),[34,35] ethylene glycol (EG),[36,37] and carbonates,[38,39] which are highly flammable and pose safety hazards. Very recently, a concentrated hydrous organic electrolyte composed of 4 mol kg^{-1} (m) hydrated $Zn(BF_4)_2$ in EG has been proposed to tackle Zn dendrite growth and water-induced parasitic reactions.[36] Compared with the aqueous counterpart, most anhydrous or hydrous organic electrolytes have lower ionic conductivity and permit limited current density and areal capacity (*e.g.*, 1 mA cm^{-2} and 1 mA h cm^{-2}) of Zn anodes, which remains far from the goal for practical applications of RZBs.[40] Besides, current oxide-based cathode materials suffer from dissolution in aqueous electrolytes, leading to rapid performance degradation.[20,41–43] It is desirable to formulate dilute hydrous organic electrolytes with lower viscosity, higher conductivity and suppressed metal dissolution whilst maintaining the intrinsic safety merits of aqueous materials. Furthermore, the development of hydrous organic electrolytes calls for more efforts to unravel the effect of

[a]*College of Chemistry & Environmental Science, Key Laboratory of Analytical Science and Technology of Hebei Province, Hebei University, Baoding 071002, P. R. China. E-mail: ningzhang@hbu.edu.cn*

[b]*Key Laboratory of Advanced Energy Materials Chemistry (Ministry of Education), College of Chemistry, Nankai University, Tianjin 300071, P. R. China. E-mail: fycheng@nankai.edu.cn*

[c]*China College of Physics and Optoelectronic Engineering, Shenzhen University, Shenzhen 518060, P. R. China*

[d]*Haihe Laboratory of Chemical Transformation, Tianjin 300071, P. R. China*

† Electronic supplementary information (ESI) available. See https://doi.org/10.1039/d2sc04143j

‡ These authors contributed equally to this work.

salts and solvents on electrolyte properties, solvation structures, interface chemistry, and Zn reversibility.

In this study, we comparatively investigate a series of hydrous organic electrolytes by combining four typical hydrated Zn-salts of $Zn(ClO_4)_2\cdot 6H_2O$, $Zn(NO_3)_2\cdot 6H_2O$, $Zn(CH_3COO)_2\cdot 2H_2O$ ($Zn(Ac)_2\cdot 2H_2O$), and $ZnSO_4\cdot 7H_2O$ and five representative organic solvents of EG, AN, trimethyl phosphate (TMP), dimethyl carbonate (DMC), and 1,2-dimethoxyethane (DME). Among them, the low-cost and fire-retardant TMP solvent endows the electrolyte with non-flammable nature, while the cost-efficient $Zn(ClO_4)_2\cdot 6H_2O$ salt exhibits good solubility in organic solvents. We demonstrate that the electrolyte structure, Zn interface chemistry, and Zn reversibility can be tuned by adjusting the Zn-salt concentration in TMP. Different from previous conception, a dilute 0.5 m $Zn(ClO_4)_2\cdot 6H_2O$ in TMP electrolyte is found to feature a H_2O-poor Zn^{2+}-solvation sheath and low water activity, thus exhibiting much higher Zn reversibility and a wider electrochemical window than the concentrated counterpart. In addition, the TMP and ClO_4^- co-participated Zn^{2+} solvation shell not only guides the uniform Zn deposition but also promotes the formation of a $Zn_3(PO_4)_2$–$ZnCl_2$-rich interphase, significantly stabilizing the Zn electrode. As a result, the Zn electrode manifests long-term cyclability over 1200 h at an areal capacity of 5 mA h cm^{-2} and a current density of 5 mA cm^{-2}. Furthermore, the designed dilute $Zn(ClO_4)_2\cdot 6H_2O$/TMP electrolyte mitigates the metal dissolution of a vanadium oxide cathode, endowing the full $Zn//Zn_{0.13}V_2O_5\cdot nH_2O$ cell with remarkable cycling stability.

Results and discussion

Electrolyte formulation and characterization

To screen hydrous organic electrolytes, we have selected four hydrated Zn-salts ($Zn(ClO_4)_2\cdot 6H_2O$, $Zn(NO_3)_2\cdot 6H_2O$, $Zn(Ac)_2\cdot 2H_2O$, and $ZnSO_4\cdot 7H_2O$) and five organic solvents (*e.g.*, EG, AN, TMP, DMC, and DME) for comparison. Among them, TMP has been employed in Li/Na/K-based batteries as a fire-retardant co-solvent.[10,44,45] As shown in Fig. 1a and S1 (ESI†), $Zn(ClO_4)_2\cdot 6H_2O$ can easily dissolve in all of the tested organic solvents to form transparent solutions. Ignition tests (Fig. 1b and S2, ESI†) demonstrate that the TMP-based electrolyte features non-flammable nature, whereas the other electrolytes based on AN, EG, DME, and DMC are highly flammable. Hydrated salts of $Zn(Ac)_2\cdot 2H_2O$ and $ZnSO_4\cdot 7H_2O$ are almost insoluble in TMP. Hydrated $Zn(NO_3)_2\cdot 6H_2O$ is soluble in TMP, but 0.5 m $Zn(NO_3)_2\cdot 6H_2O$/TMP exhibits a weak Zn^{2+} plating/stripping process mainly due to its low ionic conductivity (1.26 mS cm^{-2}, Fig. S3, ESI†). Thus, $Zn(ClO_4)_2\cdot 6H_2O$ in TMP solution has been chosen as the electrolyte for further evaluation.

A batch of hydrous organic electrolytes were prepared by adding 0.2, 0.5, 1, and 2 mol kg^{-1} $Zn(ClO_4)_2\cdot 6H_2O$ in TMP, which are denoted as 0.2, 0.5, 1, and 2 m TMP, respectively. The $Zn(ClO_4)_2\cdot 6H_2O$/TMP based electrolytes exhibit low volatility with 94% of the original weight after exposing to the atmosphere for 240 h, whereas the reference aqueous electrolyte (0.5 m $Zn(ClO_4)_2\cdot 6H_2O$ in H_2O, denoted as 0.5 m H_2O) quickly decreases to 31% after 120 h (Fig. 1c). The thermogravimetric analysis (TGA) curves in Fig. 1d reveal that TMP-based electrolytes exhibit negligible volatility up to 100 °C. In contrast, the 0.5 m H_2O counterpart displays a faster weight loss of 45% on heating to 100 °C. The high thermal stability and non-flammability endow the TMP-based hydrous organic electrolyte with considerable safety.

Fig. 1e presents the ionic conductivity and viscosity of electrolytes with *x* m $Zn(ClO_4)_2\cdot 6H_2O$ in TMP. Increasing the Zn-salt concentration significantly increases the electrolyte viscosity from 15.2 mPa s (0.5 m) to 51.8 mPa s (2 m). A relatively high ionic conductivity of 6.13 mS cm^{-1} is observed in 0.5 m TMP (Fig. S4, ESI†), higher than those of reported organic Zn-based electrolytes. Moreover, 0.5 m TMP shows a higher Zn^{2+} transference number (0.49) than the aqueous counterpart (0.28) (Fig. S5, ESI†). In addition, the dilute hydrous electrolyte manifests enhanced hydrophilicity on Zn (Fig. S6, ESI†), which favors reducing the interfacial free energy on the Zn–electrolyte interface and homogenizing the Zn^{2+} deposition.[26,28] The molar ratio of H_2O to TMP gradually increases from 0.42 in 0.5 m TMP to 1.68 in 2 m TMP (Fig. 1f). The higher H_2O content will contribute to a H_2O-rich Zn^{2+}-solvation shell, thus inevitably deteriorating the H_2O-induced side reactions on Zn, as shown later.

FTIR and Raman spectra are recorded to probe the structural evolution of electrolytes as a function of the salt concentration. As shown in Fig. 1g, the broad O–H stretching vibration (2900–3700 cm^{-1}) can be divided into three categories of H_2O molecules with different H-bonding environments: bulk H_2O with a strong H-bond (~3200 cm^{-1}), cluster H_2O with a weak H-bond (~3450 cm^{-1}), and isolated H_2O with a non-H-bond (~3560 cm^{-1}).[27,46] The fitting results of different electrolytes are provided in Fig. S7 (ESI†). Increasing the $Zn(ClO_4)_2\cdot 6H_2O$ concentration leads to enhanced population of bulk and cluster H_2O, suggesting the formation of a highly H-bonded water structure. Moreover, the H_2O bending vibration exhibits a redshift from 0.2 to 2 m TMP, indicating the H-bond reformation between H_2O molecules. The intensified strong H-bond environment of water will increase water activity and worsen water-induced interfacial side reactions.[19,46] The signals located at 1400–1500 cm^{-1} and 2800–3000 cm^{-1} are attributed to C–H bending and stretching vibrations, respectively.[32] From the Raman spectra, the P=O stretching vibration of TMP molecules experiences a blueshift from 0.2 to 0.5 m, signifying the strengthened Zn^{2+}–TMP coordination (Fig. 1h).[10,45] However, further increasing the concentration from 0.5 to 2 m renders a redshift of the P=O signal, demonstrating the replacement of TMP in the Zn^{2+}-solvation sheath by H_2O. In addition, the signal of the ClO_4^- anion[30,32,47] intensifies along with a slight blueshift as the salt concentration increases, implying the presence of ClO_4^- in the Zn^{2+}-solvation sheath (Fig. 1i).

The effect of the $Zn(ClO_4)_2\cdot 6H_2O$ concentration on the electrolyte structure was further investigated by molecular dynamics (MD) simulations and density functional theory (DFT) calculations. Fig. 2a–c present the MD snapshots and typical Zn^{2+} solvation sheaths of 0.5 m H_2O, 0.5 m TMP, and 2 m TMP, respectively. The compositions of these electrolytes for MD simulations are provided in Table S1 (ESI†). In 0.5 m TMP, the

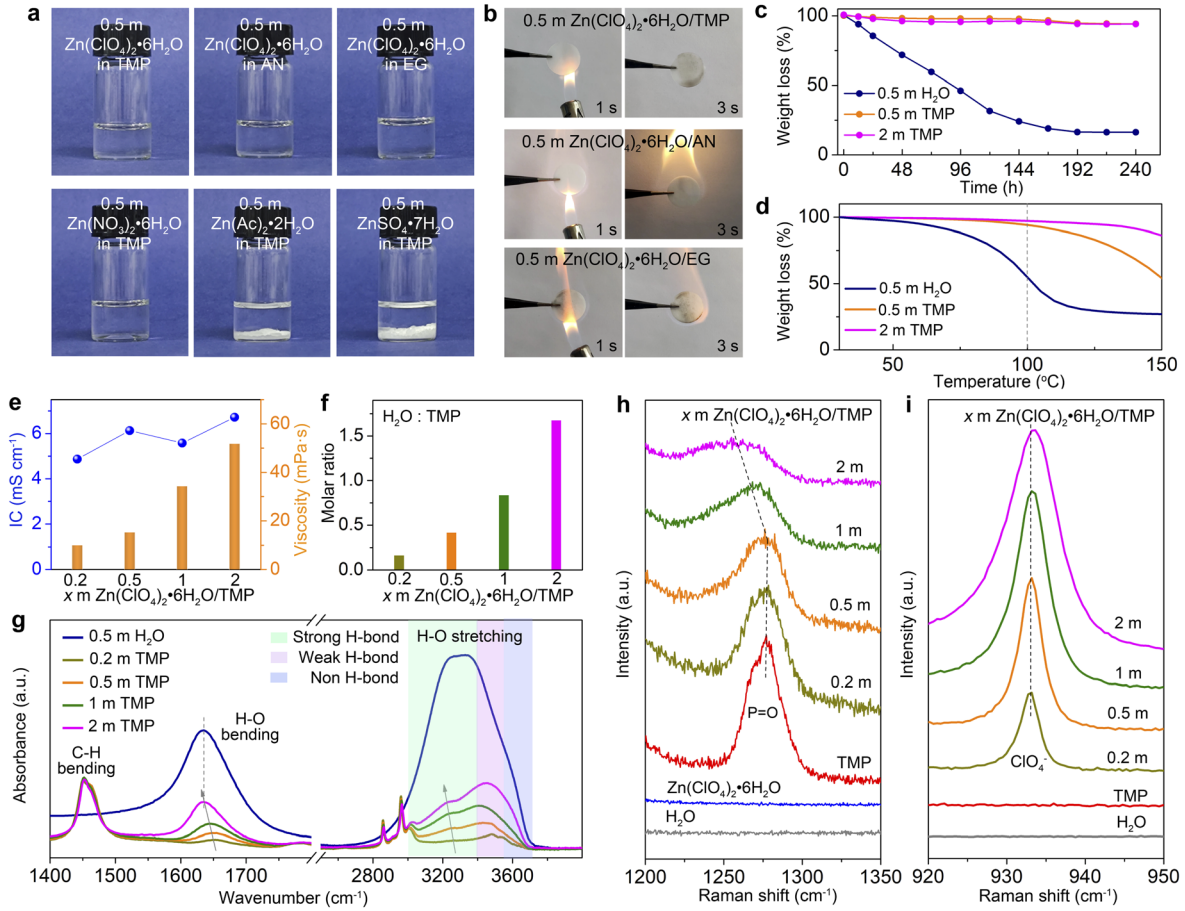

Fig. 1 Electrolyte characterization. (a) Digital photos of the prepared electrolytes. (b) Ignition tests of glass fiber separators saturated with different electrolytes composed of 0.5 m $Zn(ClO_4)_2{\cdot}6H_2O$ in TMP, AN, and EG. (c) Volatility tests of 0.5 m H_2O, 0.5 m TMP, and 2 m TMP electrolytes at room temperature. (d) TGA curves of various electrolytes from 30 to 150 °C. (e) Ionic conductivity (IC) and viscosity of *x* m $Zn(ClO_4)_2{\cdot}6H_2O$/TMP electrolytes (*x* = 0.2, 0.5, 1 and 2). (f) Molar ratio of H_2O to TMP in different electrolytes. (g) FTIR spectra and (h and i) Raman spectra of electrolytes. (h) and (i) show the P═O (TMP) stretching vibration and Cl–O (ClO_4^-) stretching vibration, respectively.

TMP solvent and ClO_4^- anion co-participate in the Zn^{2+} solvation sheath (Fig. 2b), which differs from that in 0.5 m H_2O with a typical $Zn[H_2O]_6^{2+}$ structure (Fig. 2a). In the concentrated 2 m TMP, more H_2O molecules insert into the Zn^{2+} solvation sheath to replace the solvating TMP (Fig. 2c), consistent with the aforementioned spectroscopic analyses. Radial distribution functions (RDFs) reflect the distributions of nearest-neighbor molecules, which further identify the structure evolution of electrolytes.[27,30] The primary solvation shell of Zn^{2+} is around 0.4 nm in distance. In 0.5 m H_2O, the average coordination numbers of Zn^{2+}–H_2O and Zn^{2+}–ClO_4^- are 5.8 and 0.2, respectively (Fig. 2d). In TMP-based electrolytes, besides the Zn^{2+}–H_2O signal, two peaks involving Zn^{2+}–O from Zn^{2+}–ClO_4^- and Zn^{2+}–TMP coordination appear at 0.33 and 0.36 nm, respectively (Fig. 2e). Accordingly, the primary Zn^{2+}-solvation shell in 0.5 m TMP is occupied by 0.6H_2O, 1.3 ClO_4^-, and 3.8 TMP on average, corresponding to $Zn^{2+}[H_2O]_{0.6}[ClO_4^-]_{1.3}[TMP]_{3.8}$. In contrast, a H_2O-rich Zn^{2+}-solvation shell is detected in 2 m TMP electrolyte (*i.e.*, $Zn^{2+}[H_2O]_{2.5}[ClO_4^-]_{2.3}[TMP]_{1.4}$, Fig. 2f). Since the solvating-H_2O exhibits a higher activity of reductive decomposition than the free H_2O (Fig. S8, ESI†), the water-induced side reactions would inevitably occur in the concentrated hydrous organic electrolyte.

DFT calculations show that the binding energies between two ingredients follow the order of Zn^{2+}–ClO_4^- < Zn^{2+}–TMP < Zn^{2+}–H_2O (Fig. 2g). Considering the small size and high dielectric constant ($\varepsilon = 78.5$ for H_2O *vs.* $\varepsilon = 21.6$ for TMP),[45] H_2O can favorably solvate with Zn^{2+} in the concentrated hydrous organic electrolyte. In addition, the binding energy of TMP–H_2O is lower than that of H_2O–H_2O, implying feasible formation of a H-bond between TMP and H_2O. According to MD simulations, the average H-bond number per H_2O in 0.5 m H_2O, 0.5 m TMP, and 2 m TMP is around 3.38, 0.95, and 1.35, respectively (Fig. 2h). The lower value of TMP electrolytes suggests a weakened water activity. Furthermore, the lower adsorption energy of TMP (−0.48 eV) than that of H_2O (−0.38 eV) reveals that TMP preferentially absorbs on Zn, which favors constraining random Zn^{2+} deposition (Fig. 2i).

Zn surface/interface chemistry in different electrolytes

The Zn plating behavior in H_2O and TMP-based electrolytes is probed in symmetric Zn//Cu cells using optical microscopy. In

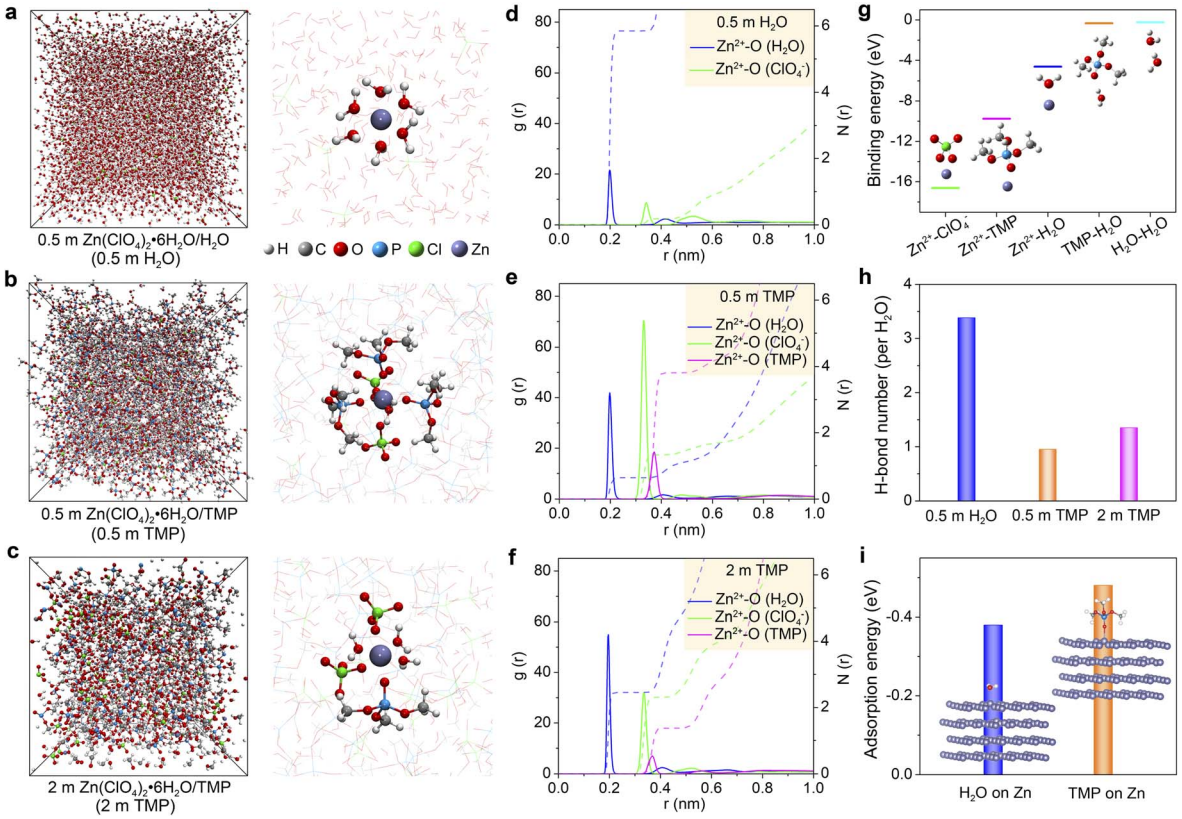

Fig. 2 Theoretical computations on the electrolyte structure. (a–c) Snapshots of MD simulated cells (right) and typical Zn^{2+}-solvation structures (left) for (a) 0.5 m H_2O, (b) 0.5 m TMP, and (c) 2 m TMP. (d–f) RDF plots for Zn^{2+}–O (H_2O), Zn^{2+}–O (TMP), and Zn^{2+}–O (ClO_4^-) pairs, and corresponding coordination numbers in (d) 0.5 m H_2O, (e) 0.5 m TMP, and (f) 2 m TMP. (g) Binding energies between any two ingredients in TMP-based electrolytes. (h) The H-bond number per H_2O. (i) Adsorption energies of H_2O and TMP molecules on the Zn surface.

0.5 m H_2O, non-uniform Zn plating sites emerge after 20 min, and they gradually grow into dendritic Zn protrusions after 40 min at 10 mA cm^{-2} (Fig. 3a). In stark contrast, the 0.5 m TMP electrolyte enables a uniform and compact Zn plating (Fig. 3b). The chemical stability of Zn in electrolytes is compared by immersing Zn foil in H_2O and TMP-based electrolytes (Fig. 3c–f and S9, ESI†). Massive flake-like and spherical by-products are observed on the Zn surface after soaking for 3 days in 0.5 m H_2O (Fig. 3c). In addition, the XRD signals of ZnO and $Zn_4ClO_4(OH)_7$ are detected on Zn after soaking in the aqueous electrolyte (Fig. 3f). By contrast, the Zn foil after soaking in 0.5 m TMP maintains a compact and smooth surface without any discernible by-product (Fig. 3d and f), identifying the effective suppression of water-induced side reactions on Zn by using the dilute hydrous TMP electrolyte. However, a small amount of $Zn_4ClO_4(OH)_7$ with slight corrosion is observed after soaking Zn in the concentrated 2 m TMP (Fig. 3e and f). The by-product formation and Zn corrosion are mainly induced by the H_2 evolution reaction ($2H_2O + 2e^- \rightarrow H_2 + 2OH^-$; $Zn \rightarrow Zn^{2+} + 2e^-$), which increases the local pH near Zn and thus triggers the precipitation reaction of OH^- with Zn^{2+}, ClO_4^-, and H_2O (*e.g.*, $Zn^{2+} + 2OH^- \rightarrow ZnO + H_2O$; $4Zn^{2+} + 7OH^- + 4ClO_4^- \rightarrow Zn_4ClO_4(OH)_7$).[20,27,30] The different by-products in H_2O-based and TMP-based electrolytes may be due to the difference in the Zn^{2+} solvation shell, where a ClO_4^--rich Zn^{2+} solvation shell in 2 m TMP would favor forming the $Zn_4ClO_4(OH)_7$ by-product.

The surface and interphase chemistry on the cycled Zn electrode in 0.5 m TMP were analyzed using X-ray photoelectron spectroscopy (XPS) with Ar^+ sputtering (Fig. 3g). The cycled Zn was harvested from a Zn//Zn cell after 10 cycles at 1 mA cm^{-2}. On the top surface (before sputtering), there are strong C signals involving organic components (C–C/C–H and C–O) and organic RPO_3^- (R represents alkyl) species, which is ascribed to the incomplete reduction products of the organic TMP solvent.[48,49] Moreover, the interphase contains the ClO_4^- component, which arises from the incomplete reduction of ClO_4^- or a trace salt residue on Zn. With the Ar^+ sputtering, the signal of the organic species is apparently decreased, whereas inorganic components of $Zn_3(PO_4)_2$ (134 eV)[48,49] and $ZnCl_2$ (200 eV)[20] significantly intensify, confirming the decomposition of Zn^{2+}–TMP and Zn^{2+}–ClO_4^- complexes. After 60 s etching, the $Zn_3(PO_4)_2$ content increases from 29.9% to 65.8%, and the $ZnCl_2$ content increases from 4.5% to 49.7%, indicating the enrichment of inorganic species in the inner SEI layer. $Zn_3(PO_4)_2$ and $ZnCl_2$ have been identified as the primary rigid-frame materials in the SEI, wherein they can homogenize Zn^{2+} diffusion and suppress Zn corrosion.[12,20,49] Note that $ZnCl_2$ is almost insoluble in the 0.5 m TMP electrolyte (Fig. S10, ESI†).

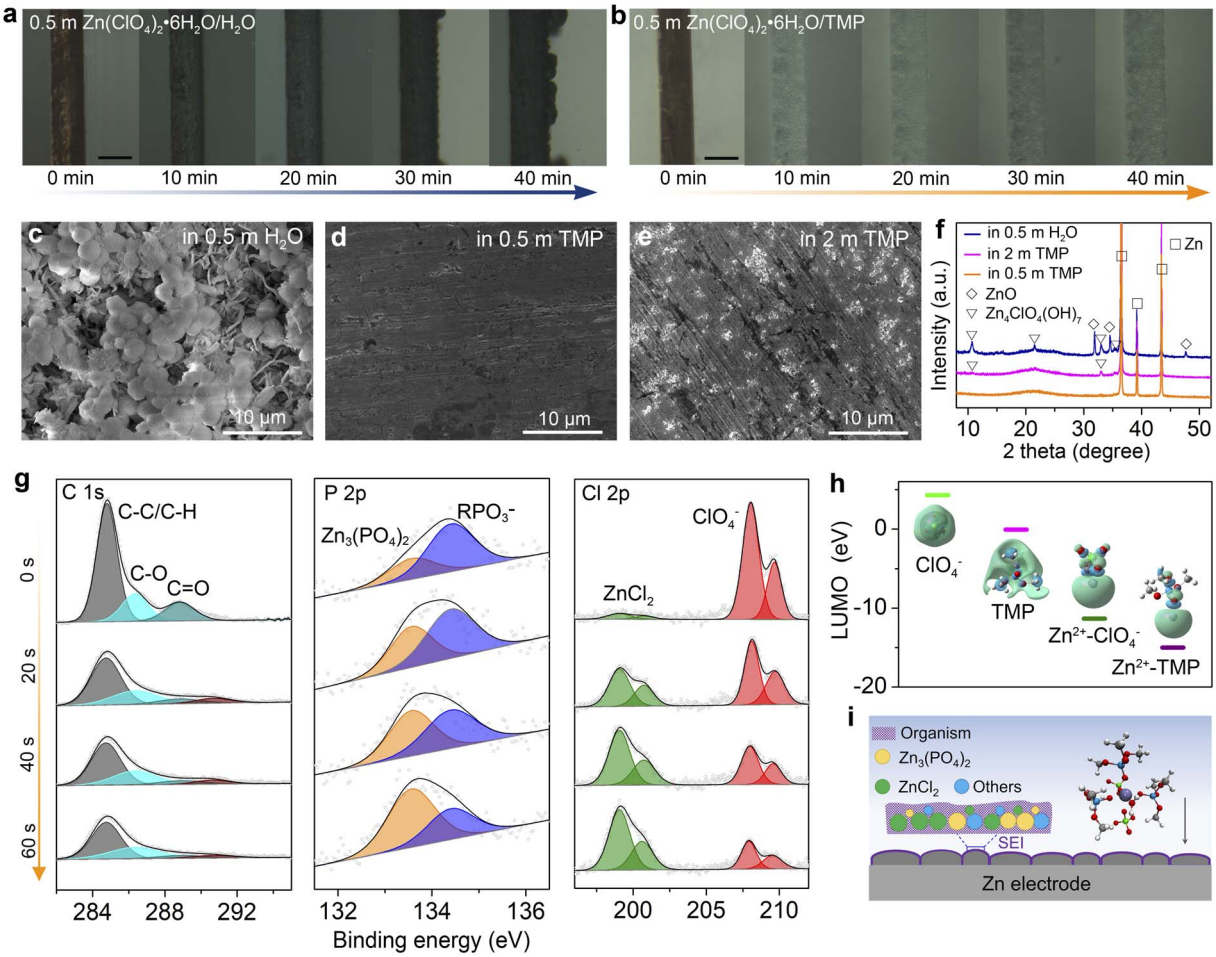

Fig. 3 Investigations on Zn surface/interface chemistry. (a and b) *In situ* optical microscope images of Zn electro-plating in (a) 0.5 m H_2O and (b) 0.5 m TMP. Scale bar 100 μm. (c–e) SEM images of Zn electrodes after soaking in (c) 0.5 m H_2O, (d) 0.5 m TMP, and (e) 2 m TMP for 3 days. (f) XRD patterns of Zn electrodes after soaking in different electrolytes. (g) XPS spectra of C 1s, P 2p, and Cl 2p regions of the cycled Zn electrode in 0.5 m TMP. (h) LUMO energy levels with corresponding isosurfaces of free ClO_4^-, free TMP, Zn^{2+}–ClO_4^- and Zn^{2+}–TMP coordination. (i) Schematic illustration of the interphase on Zn in 0.5 m TMP.

DFT calculations further reveal that the lowest unoccupied molecular orbital (LUMO) energies of Zn^{2+}–TMP and Zn^{2+}–ClO_4^- coordinations are lower than those of free TMP and ClO_4^- (Fig. 3h), demonstrating the preferred electron reception of Zn^{2+}–TMP and Zn^{2+}–ClO_4^- from the anode. The electron feasibly transfers from the cation to the solvent/anion *via* the cation–solvent/anion unit, rendering the reductive decomposition of the solvent/anion and the presence of decomposed species in the SEI.[27] Thus, the unique Zn^{2+} solvation sheath with the co-participation of TMP and ClO_4^- contributes to SEI formation on Zn. As illustrated in Fig. 3i, the *in situ* generated SEI, which is mainly composed of an organic-rich outer layer and a $Zn_3(PO_4)_2$–$ZnCl_2$ rich inner layer, can suppress the continuous parasitic reactions to stabilize the Zn electrode.

Electrochemical reversibility of Zn electrodes in different electrolytes

Fig. 4a compares the cyclic voltammograms (CVs) of Zn//Ti cells with different electrolytes from −0.3 to 3.0 V at 1 mV s^{-1}. The redox couple located between −0.3 and 0.3 V is associated with the Zn^{2+} stripping/plating process. The 0.5 m H_2O electrolyte exhibits a higher current response of Zn^{2+} stripping/plating because of high ionic conductivity but shows a rapid current decrease in the following cycles due to H_2O-induced side reactions. Additionally, the severe O_2 evolution appears at 2.5 V. In sharp contrast, the 0.5 m TMP electrolyte manifests a stable Zn^{2+} stripping/plating and achieves high anodic stability up to 3.0 V with negligible O_2 evolution. In comparison, a slight decrease of current involving the Zn plating/stripping is observed in 2 m TMP after the first cycle, demonstrating reduced reversibility. An apparent O_2 evolution is detected at 2.75 V, suggesting high H_2O activity in the concentrated electrolyte.

The coulombic efficiency (CE) of Zn^{2+} stripping/plating in different electrolytes was quantified using a 'reservoir half-cell' protocol.[9] As shown in Fig. 4b, the Zn//Cu cells were first subjected to two cycles of charge/discharge at 1 mA cm^{-2} with an areal capacity of 1 mA h cm^{-2} and a cut-off voltage of 0.5 V to

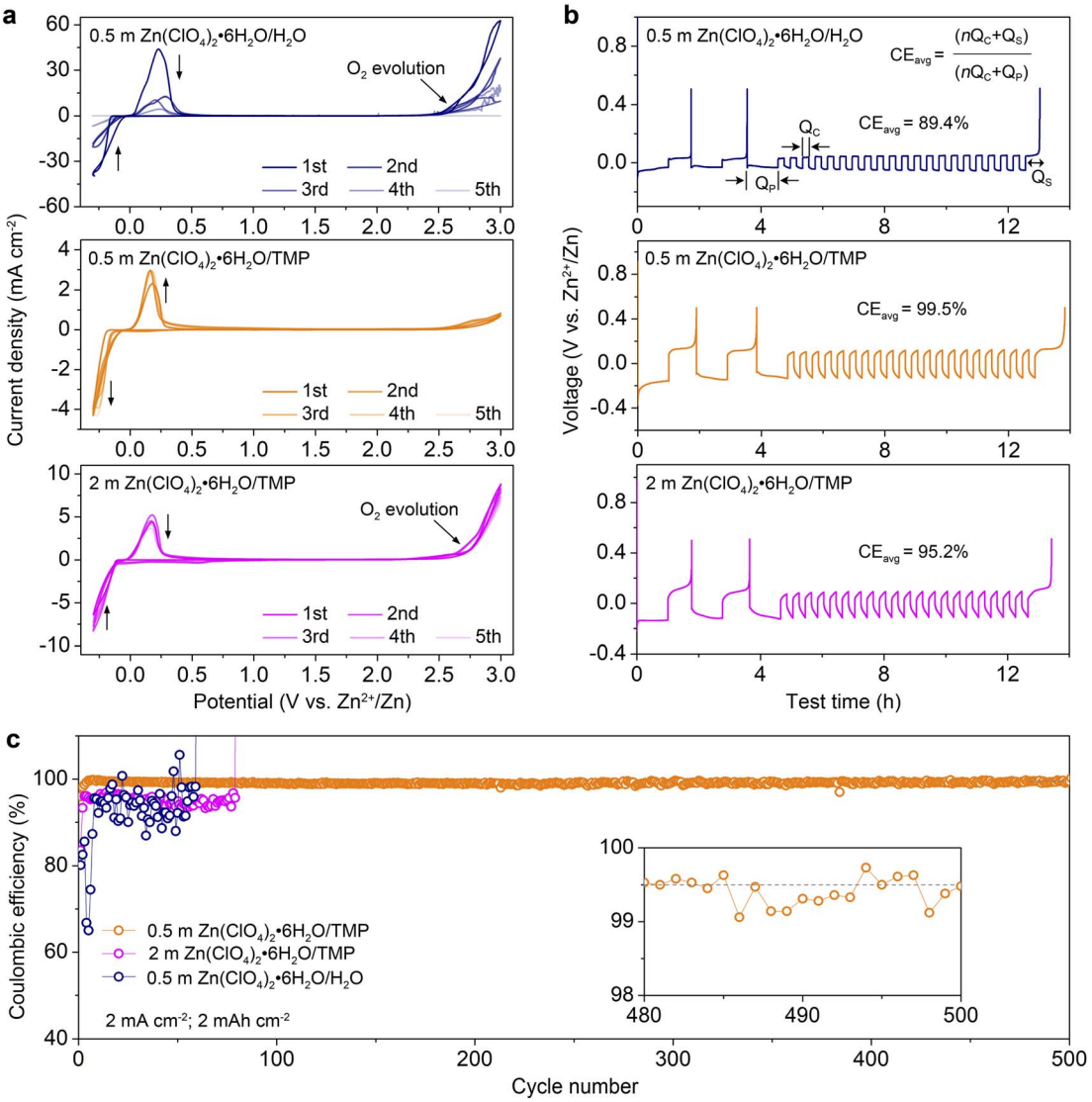

Fig. 4 Electrochemical reversibility of the Zn electrode. (a) CV profiles of Zn//Ti cells in different electrolytes from −0.3 to 3.0 V at 1 mV s^{-1}. (b) Voltage profiles of Zn//Cu cells in different electrolytes using a 'reservoir half-cell' method. (c) Zn plating/stripping CE of Zn//Cu cells with electrolytes of 0.5 m H_2O, 0.5 m TMP, and 2 m TMP at 2 mA cm^{-2} and 2 mA h cm^{-2}. The inset magnifies the profile within 480–500 cycles.

mitigate the substrate effects. Afterwards, 1 mA h cm^{-2} Zn (Q_P) was electro-plated on the Cu substrate as a Zn reservoir, which was then cycled at a fixed plating capacity of 0.2 mA h cm^{-2} (Q_C). After n cycles (*e.g.*, 20), this cell was fully charged to 0.5 V to strip all removable Zn (Q_S). According to the equation shown in Fig. 4B, 0.5 m TMP enables a much higher average CE of 99.5% than 0.5 m H_2O (89.4%), 1 m TMP (98.6%, Fig. S11, ESI†), and 2 m TMP (95.2%). Although 0.2 m TMP exhibits a respectable average CE of 99.4%, it shows a higher voltage polarization than that of 0.5 m TMP (Fig. S12, ESI†). Taking into consideration the comprehensive factors of ionic conductivity, viscosity, reversibility, the electrochemical window and cost, the dilute 0.5 m TMP is selected as the optimized electrolyte.

Besides, the dilute electrolyte can well support the stable cycling of the asymmetric Zn//Cu cell at 2 mA cm^{-2} with 2 mA h cm^{-2} (Fig. 4c and S13, ESI†). Impressively, the cell with 0.5 m TMP electrolyte shows a much higher initial CE of 95.9%, significantly outperforming those with 0.5 m H_2O (80.2%) and 2 m TMP (83.6%). Additionally, the CE in 0.5 m TMP stabilizes at an average value of 99.5% over 500 cycles. In contrast, the cell using 0.5 m H_2O displays unstable cycling with fluctuated CE values due to severe H_2O-induced side reactions. The 2 m TMP moderately improves the reversibility but displays a short lifespan of 80 cycles with a lower CE below 97%. In comparison with reported Zn-based electrolytes (Table S2, ESI†), the as-designed 0.5 m TMP manifests superior performance in terms of initial and stable CEs.

The electrochemical stability of Zn electrodes in different electrolytes was further evaluated using symmetric Zn//Zn cells. As shown in Fig. 5a and b, the cell in 0.5 m TMP can be stably cycled over 3200 h at a current density of 1 mA cm^{-2} and an areal capacity of 1 mA h cm^{-2}. For comparison, the aqueous

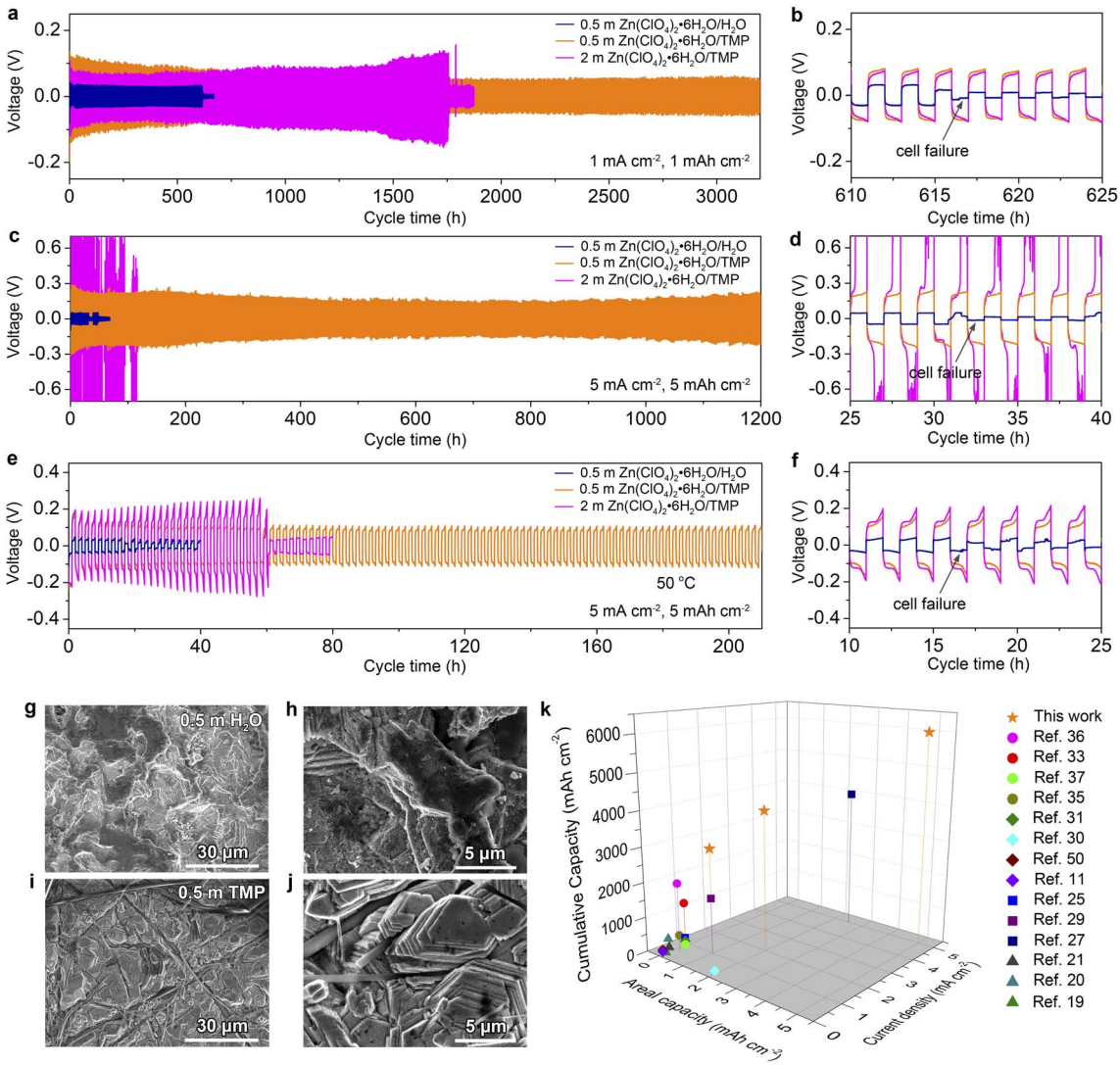

Fig. 5 Electrochemical and morphological characterization of Zn electrodes. (a–d) Galvanostatic room-temperature cycling performance of Zn//Zn cells with different electrolytes at (a and b) 1 mA cm^{-2}; 1 mA h cm^{-2} and (c and d) 5 mA cm^{-2}; 5 mA h cm^{-2}. (e and f) Cycling performance of Zn//Zn cells at 5 mA cm^{-2} and 5 mA h cm^{-2} at 50 °C. (g–j) SEM images of cycled Zn in (g and h) 0.5 m H_2O and (i and j) 0.5 m TMP electrolytes. (k) Comparison of this work with reported electrolytes for RZBs in terms of performance metrics such as cumulative capacity, areal capacity, and current density.

electrolyte gives rise to a short-circuit cell failure after 610 h, which is mainly caused by the dendrite growth and water-induced parasitic reactions on Zn. The concentrated 2 m TMP results in a shorter lifespan of 1750 h than that of the dilute one (Fig. S14, ESI†). Even at 5.0 mA h cm^{-2} and 5.0 mA cm^{-2}, the cell with 0.5 m TMP manifests cycling stability over 1200 h with steady voltage curves (Fig. S15, ESI†) and significantly outperforms the 0.5 m H_2O cell experiencing failure after only 30 h (Fig. 5c and d). At 5 mA cm^{-2}, note that concentrated 2 m TMP incurs a large voltage polarization because of high electrolyte viscosity, while too diluted 0.2 m TMP cannot support stable cycling of Zn due to low conductivity (Fig. S16, ESI†). In addition, the Zn//Zn cell in 0.5 m TMP achieves a good rate performance even at a high current of 10 mA cm^{-2} (Fig. S17, ESI†). Furthermore, the formulated 0.5 m TMP endows the Zn//Zn cell with much improved high-temperature adaptability (50 °C) as compared to the counterparts 0.5 m H_2O and 2 m TMP (Fig. 5e and f).

The cycled Zn electrodes were characterized by SEM and XRD to further assess the effect of dilute hydrous organic electrolyte on Zn stabilization. As shown in Fig. 5g and h, the Zn electrode dismantled from Zn//Zn cells after 100 cycles at 1 mA cm^{-2} in 0.5 m H_2O presents a rough surface. In contrast, a compact and horizontal Zn surface is observed in 0.5 m TMP (Fig. 5i and j), while corrosion can be observed in 2 m TMP (Fig. S18, ESI†). Phase analysis further reveals indiscernible formation of a by-product in 0.5 m TMP but clear generation of ZnO in 0.5 m H_2O and $Zn_4ClO_4(OH)_7$ in 2 m TMP (Fig. S19, ESI†). Furthermore, the cycled Zn electrode in 0.5 m TMP exhibits a higher intensity ratio of Zn(002) to Zn(100) than that in the aqueous counterpart (6.28 *vs.* 4.93), contributing to the dendrite-free behavior in 0.5 m TMP. In addition, the formulated 0.5 m

TMP in this study compares favorably with recently reported electrolytes for Zn-based battery chemistries such as concentrated hydrous organic electrolytes,[36] anhydrous organic electrolytes,[33,35,37] deep eutectic electrolytes,[11,30,31,50] hybrid aqueous/organic electrolytes,[25,27,29] and concentrated dual salt electrolytes[19–21] (Fig. 5k). The dilute 0.5 m $Zn(ClO_4)_2 \cdot 6H_2O$/TMP electrolyte delivers an impressive cumulative capacity at a high rate (*i.e.*, 6000 mA h cm^{-2} at 5 mA cm^{-2}), standing out from the state-of-the-art Zn-based electrolytes.

Electrochemical performance of full Zn batteries

In addition to boosting Zn reversibility, the designed dilute hydrous organic electrolyte with low water activity can also improve the stability of vanadium oxide-based cathodes by suppressing the dissolution in aqueous media. Taking a conventional V-based cathode of $Zn_{0.13}V_2O_5 \cdot nH_2O$ as an example (denoted as ZVO, Fig. S20, ESI†), we compare its cycling performances and voltage profiles in different electrolytes at 0.2 A g^{-1} (Fig. 6a–c). The Zn//0.5 m TMP//ZVO full cell exhibits an initial capacity increase, which is mainly ascribed to the activation process as confirmed by the decreased charge-transfer resistance during cycling (Fig. S21, ESI†). After 50 cycles, it achieves a stable capacity of 299.5 mA h g^{-1}, indicating favorable compatibility between the 0.5 m TMP electrolyte and ZVO cathode. In contrast, the ZVO cathode in 0.5 m H_2O experiences a rapid capacity decay during cycling and delivers a low capacity of 155.5 mA h g^{-1} with 45.3% capacity retention after 100 cycles (Fig. 6c). This poor cyclability can be attributed to the dissolution of vanadium from the cathode and the interfacial side reactions on Zn. In addition, the 0.5 m TMP electrolyte enables considerable rate stability with average reversible capacities of 262.4, 218.7, and 155.9 mA h g^{-1} at 0.5, 1, and 2 A g^{-1}, respectively, exceeding those of the 0.5 m H_2O counterpart (Fig. 6d and S22, ESI†). Remarkably, the average capacity in 0.5 m TMP can recover to 295.4 mA h g^{-1} (in the 150th cycle) as the current returns to 0.2 A g^{-1}, again outperforming that in 0.5 m H_2O.

The advantage of the TMP-based electrolyte was also assessed by monitoring the open-circuit voltage evolution of a fully charged cell, which was subsequently discharged after 24 h of rest and tested by conducting the process twice (Fig. 6e). Considerable CE values of 98.1% and 99.1% are achieved in 0.5 m TMP for the first and second process, respectively, much

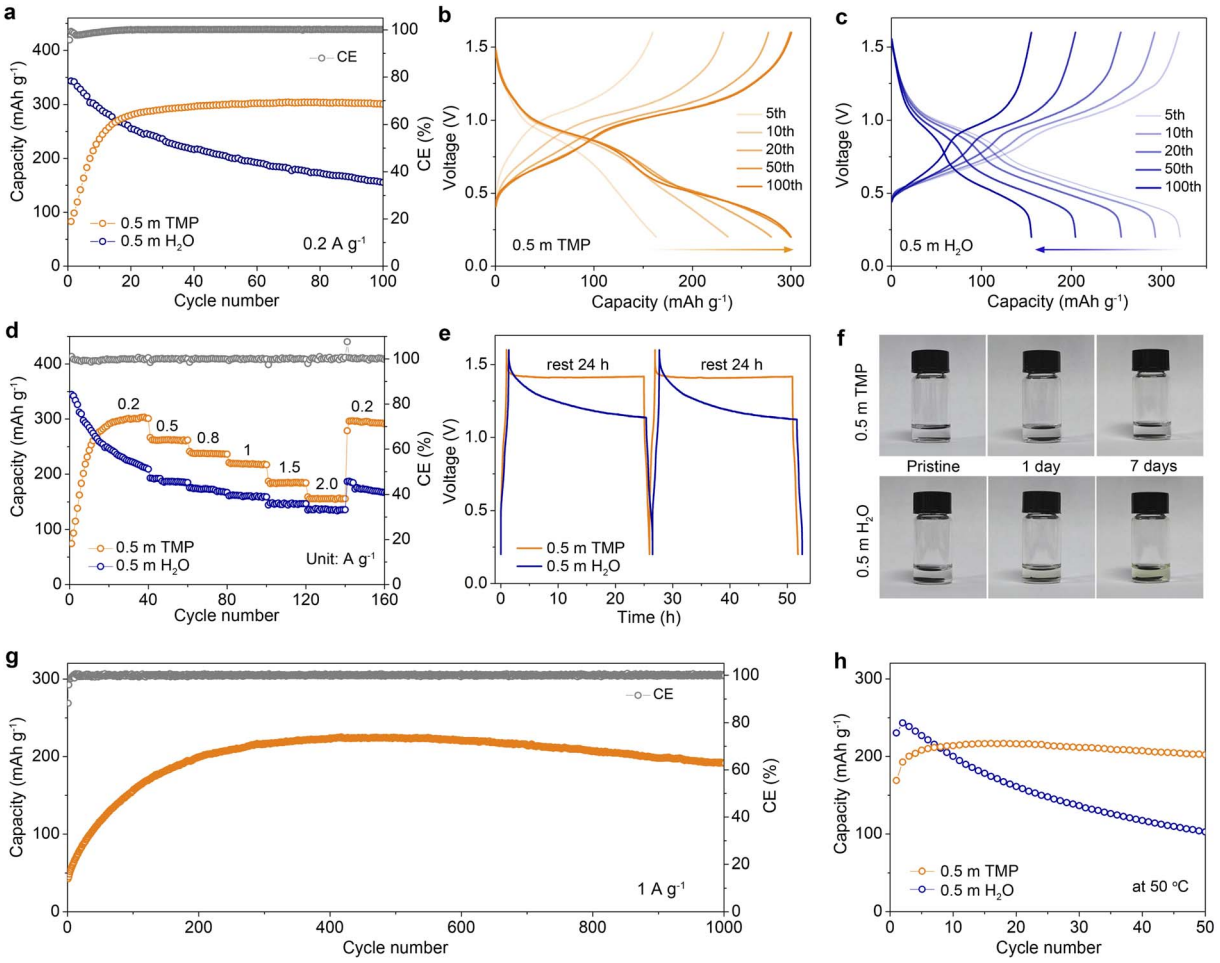

Fig. 6 Electrochemical performance of full Zn batteries. (a) Cycling performances at 0.2 A g^{-1} and the corresponding voltage profiles for (b) 0.5 m H_2O and (c) 0.5 m TMP. (d) Rate capability. (e) Comparison of storage performance. (f) Optical images of the ZVO cathode soaked in 0.5 m H_2O and 0.5 m TMP for different times. (g) Extended cycling behavior of the 0.5 m TMP-based cell at 1 A g^{-1}. (h) Cycling stability at 0.5 A g^{-1} at 50 °C.

higher than those in 0.5 m H_2O (79.6% and 77.9%). Moreover, the cell using 0.5 m TMP exhibits a smaller voltage drop (~0.18 V) after 24 h storage than that with 0.5 m H_2O (~0.47 V). To intuitively identify the dissolution of the active material in electrolytes, static soaking of ZVO cathodes was performed in different media (Fig. 6f). The 0.5 m TMP electrolyte remains colorless and transparent even after 7 days, whereas 0.5 m H_2O turns light yellow after only 1 day. The significant suppression of ZVO dissolution contributes to the stable cycling of a full battery. In addition, the ZVO cathode with 0.5 m TMP achieves a reversible capacity of 223.9 mA h g^{-1} after 400 cycles and sustains a remarkable capacity retention of 82% with a nearly 100% CE after 1000 cycles at 1 A g^{-1} (Fig. 6g and S23, ESI†). Impressively, the 0.5 m TMP endows the cell with cycling stability at 0.5 A g^{-1} at a high operating temperature of 50 °C, in contrast to fast capacity decay in the aqueous cell (Fig. 6h and S24, ESI†). To further evaluate the potential for practical applications, we design the full battery coupling an ultrathin Zn anode (20 μm; 11.7 mA h cm^{-2}) with a high mass loading VOH cathode (18.4 mg cm^{-2}, Fig. S25, ESI†). This Zn//ZVO full battery manifests good cycling stability and delivers a reversible capacity of 5.22 mA h cm^{-2} (the 50th cycle), corresponding to a negative-to-positive capacity (N/P) ratio of 2.24.

Conclusions

In summary, we report a non-flammable, dilute, and hydrous organic electrolyte composed of hydrated $Zn(ClO_4)_2 \cdot 6H_2O$ salt and fire-retardant TMP solvent for rechargeable Zn batteries. This electrolyte circumvents the issues of Zn electrodes such as H_2 evolution, Zn corrosion, and dendrite formation in common aqueous electrolytes. The electrolyte structure, Zn interface chemistry, and Zn reversibility can be regulated by adjusting the Zn-salt concentration in TMP. The dilute 0.5 m TMP electrolyte is found to feature a H_2O-poor Zn^{2+}-solvation sheath and low water activity and exhibits a wider electrochemical window and a much higher Zn reversibility than the concentrated counterpart. Additionally, the unique Zn^{2+} solvation shell with the involvement of TMP and ClO_4^- not only enables a uniform Zn plating but also promotes the *in situ* formation of the $Zn_3(PO_4)_2$–$ZnCl_2$-rich interphase layer, contributing to a compact, dendrite-free, and corrosion-free Zn electrode. The formulated 0.5 m TMP allows a high Zn plating/stripping CE of 99.5% over 500 cycles in the Zn//Cu cell (2 mA h cm^{-2} at 2 mA cm^{-2}) and sustains extended durability over 1200 h in the Zn//Zn cell (5 mA h cm^{-2} at 5 mA cm^{-2}). Additionally, the 0.5 m TMP electrolyte suppresses the dissolution of the vanadium oxide cathode and enables a stable operation at high temperature (50 °C). This work broadens the horizon of dilute and non-flammable electrolytes to stabilize Zn electrodes and would guide the design of hydrous organic electrolytes for metallic batteries.

Data availability

All experimental and computational data associated with this article have been included in the main text and ESI.†

Author contributions

N. Z. and F. C. proposed the concept and supervised the work; G. M. and N. Z. carried out the experimental design, characterization and electrochemical measurement; L. M. performed the theoretical simulations; G. M. and W. Y. prepared the cathode materials; N. Z. and F. C. wrote and revised the paper.; W. Y., K. Q., M. L., and X. N. helped to discuss and analyze the data; all authors discussed and revised the manuscript.

Conflicts of interest

There are no conflicts to declare.

Acknowledgements

This work was supported by the National Natural Science Foundation of China (22075067 and 21925503), Natural Science Foundation of Hebei Province (B2020201001), Young Elite Scientists Sponsorship Program by CAST (2021QNRC001), the Haihe Laboratory of Sustainable Chemical Transformations (CYZC202110) and Research Innovation Team of College of Chemistry and Environmental Science of Hebei University (hxkytd2102).

References

1 S. Liu, R. Zhang, J. Mao, Y. Zhao, Q. Cai and Z. Guo, *Sci. Adv.*, 2022, **8**, eabn5097.
2 L. E. Blanc, D. Kundu and L. F. Nazar, *Joule*, 2020, **4**, 771–799.
3 Z. Liu, Y. Huang, Y. Huang, Q. Yang, X. Li, Z. Huang and C. Zhi, *Chem. Soc. Rev.*, 2020, **49**, 180–232.
4 P. Ruan, S. Liang, B. Lu, H. J. Fan and J. Zhou, *Angew. Chem., Int. Ed.*, 2022, **61**, e202200598.
5 N. Zhang, X. Chen, M. Yu, Z. Niu, F. Cheng and J. Chen, *Chem. Soc. Rev.*, 2020, **49**, 4203–4219.
6 N. Dong, F. Zhang and H. Pan, *Chem. Sci.*, 2022, **13**, 8243–8252.
7 D. Chao, W. Zhou, F. Xie, C. Ye, H. Li, M. Jaroniec and S.-Z. Qiao, *Sci. Adv.*, 2020, **6**, eaba4098.
8 J. Shin, J. Lee, Y. Park and J. W. Choi, *Chem. Sci.*, 2020, **11**, 2028–2044.
9 L. Ma, M. A. Schroeder, O. Borodin, T. P. Pollard, M. S. Ding, C. Wang and K. Xu, *Nat. Energy*, 2020, **5**, 743–749.
10 Z. Zeng, V. Murugesan, K. S. Han, X. Jiang, Y. Cao, L. Xiao, X. Ai, H. Yang, J.-G. Zhang, M. L. Sushko and J. Liu, *Nat. Energy*, 2018, **3**, 674–681.
11 H. Qiu, X. Du, J. Zhao, Y. Wang, J. Ju, Z. Chen, Z. Hu, D. Yan, X. Zhou and G. Cui, *Nat. Commun.*, 2019, **10**, 5374.
12 X. Zeng, J. Mao, J. Hao, J. Liu, S. Liu, Z. Wang, Y. Wang, S. Zhang, T. Zheng, J. Liu, P. Rao and Z. Guo, *Adv. Mater.*, 2021, **33**, 2007416.
13 Y. Chu, S. Zhang, S. Wu, Z. Hu, G. Cui and J. Luo, *Energy Environ. Sci.*, 2021, **14**, 3609–3620.
14 Z. Cai, Y. Ou, B. Zhang, J. Wang, L. Fu, M. Wan, G. Li, W. Wang, L. Wang, J. Jiang, Z. W. Seh, E. Hu, X.-Q. Yang, Y. Cui and Y. Sun, *J. Am. Chem. Soc.*, 2021, **143**, 3143–3152.

15 H. Yang, Y. Qiao, Z. Chang, H. Deng, X. Zhu, R. Zhu, Z. Xiong, P. He and H. Zhou, *Adv. Mater.*, 2021, **33**, 2102415.
16 G. Liang, J. Zhu, B. Yan, Q. Li, A. Chen, Z. Chen, X. Wang, B. Xiong, J. Fan, J. Xu and C. Zhi, *Energy Environ. Sci.*, 2022, **15**, 1086–1096.
17 H. Liu, J.-G. Wang, W. Hua, L. Ren, H. Sun, Z. Hou, Y. Huyan, Y. Cao, C. Wei and F. Kang, *Energy Environ. Sci.*, 2022, **15**, 1872–1881.
18 X. Nie, L. Miao, W. Yuan, G. Ma, S. Di, Y. Wang, S. Shen and N. Zhang, *Adv. Funct. Mater.*, 2022, **32**, 2203905.
19 F. Wang, O. Borodin, T. Gao, X. Fan, W. Sun, F. Han, A. Faraone, J. A. Dura, K. Xu and C. Wang, *Nat. Mater.*, 2018, **17**, 543–549.
20 Y.-P. Zhu, J. Yin, X. Zheng, A.-H. Emwas, Y. Lei, O. F. Mohammed, Y. Cui and H. N. Alshareef, *Energy Environ. Sci.*, 2021, **14**, 4463–4473.
21 M. Yang, J. Zhu, S. Bi, R. Wang and Z. Niu, *Adv. Mater.*, 2022, **34**, 2201744.
22 X. Ji, *eScience*, 2021, **1**, 99–107.
23 C. Li, W. Yuan, C. Li, H. Wang, L. Wang, Y. Liu and N. Zhang, *Chem. Commun.*, 2021, **57**, 4319–4322.
24 R. Qin, Y. Wang, M. Zhang, Y. Wang, S. Ding, A. Song, H. Yi, L. Yang, Y. Song, Y. Cui, J. Liu, Z. Wang, S. Li, Q. Zhao and F. Pan, *Nano Energy*, 2021, **80**, 105478.
25 L. Cao, D. Li, E. Hu, J. Xu, T. Deng, L. Ma, Y. Wang, X.-Q. Yang and C. Wang, *J. Am. Chem. Soc.*, 2020, **142**, 21404–21409.
26 J. Hao, L. Yuan, C. Ye, D. Chao, K. Davey, Z. Guo and S.-Z. Qiao, *Angew. Chem., Int. Ed.*, 2021, **60**, 7366–7375.
27 Y. Dong, L. Miao, G. Ma, S. Di, Y. Wang, L. Wang, J. Xu and N. Zhang, *Chem. Sci.*, 2021, **12**, 5843–5852.
28 G. Ma, L. Miao, Y. Dong, W. Yuan, X. Nie, S. Di, Y. Wang, L. Wang and N. Zhang, *Energy Storage Mater.*, 2022, **47**, 203–210.
29 F. Ming, Y. Zhu, G. Huang, A.-H. Emwas, H. Liang, Y. Cui and H. N. Alshareef, *J. Am. Chem. Soc.*, 2022, **144**, 7160–7170.
30 W. Yang, X. Du, J. Zhao, Z. Chen, J. Li, J. Xie, Y. Zhang, Z. Cui, Q. Kong, Z. Zhao, C. Wang, Q. Zhang and G. Cui, *Joule*, 2020, **4**, 1557–1574.
31 X. Lin, G. Zhou, M. J. Robson, J. Yu, S. C. T. Kwok and F. Ciucci, *Adv. Funct. Mater.*, 2022, **32**, 2109322.
32 Y. Dong, S. Di, F. Zhang, X. Bian, Y. Wang, J. Xu, L. Wang, F. Cheng and N. Zhang, *J. Mater. Chem. A*, 2020, **8**, 3252–3261.
33 A. Naveed, H. Yang, J. Yang, Y. Nuli and J. Wang, *Angew. Chem., Int. Ed.*, 2019, **58**, 2760–2764.
34 C. Pan, R. Zhang, R. G. Nuzzo and A. A. Gewirth, *Adv. Energy Mater.*, 2018, **8**, 1800589.
35 N. Zhang, Y. Dong, Y. Wang, Y. Wang, J. Li, J. Xu, Y. Liu, L. Jiao and F. Cheng, *ACS Appl. Mater. Interfaces*, 2019, **11**, 32978–32986.
36 D. Han, C. Cui, K. Zhang, Z. Wang, J. Gao, Y. Guo, Z. Zhang, S. Wu, L. Yin, Z. Weng, F. Kang and Q.-H. Yang, *Nat. Sustain.*, 2022, **5**, 205–213.
37 V. Verma, R. M. Chan, L. Jia Yang, S. Kumar, S. Sattayaporn, R. Chua, Y. Cai, P. Kidkhunthod, W. Manalastas and M. Srinivasan, *Chem. Mater.*, 2021, **33**, 1330–1340.
38 S.-D. Han, N. N. Rajput, X. Qu, B. Pan, M. He, M. S. Ferrandon, C. Liao, K. A. Persson and A. K. Burrell, *ACS Appl. Mater. Interfaces*, 2016, **8**, 3021–3031.
39 X. Qiu, N. Wang, X. Dong, J. Xu, K. Zhou, W. Li and Y. Wang, *Angew. Chem., Int. Ed.*, 2021, **60**, 21025–21032.
40 L. Ma, J. Vatamanu, N. T. Hahn, T. P. Pollard, O. Borodin, V. Petkov, M. A. Schroeder, Y. Ren, M. S. Ding, C. Luo, J. L. Allen, C. Wang and K. Xu, *Proc. Natl. Acad. Sci. U.S.A.*, 2022, **119**, e2121138119.
41 X. Liu, H. Zhang, D. Geiger, J. Han, A. Varzi, U. Kaiser, A. Moretti and S. Passerini, *Chem. Commun.*, 2019, **55**, 2265–2268.
42 Z. Wang, M. Zhou, L. Qin, M. Chen, Z. Chen, S. Guo, L. Wang, G. Fang and S. Liang, *eScience*, 2022, **2**, 209–218.
43 N. Zhang, Y. Dong, M. Jia, X. Bian, Y. Wang, M. Qiu, J. Xu, Y. Liu, L. Jiao and F. Cheng, *ACS Energy Lett.*, 2018, **3**, 1366–1372.
44 J. Wang, Y. Yamada, K. Sodeyama, E. Watanabe, K. Takada, Y. Tateyama and A. Yamada, *Nat. Energy*, 2018, **3**, 22–29.
45 S. Liu, J. Mao, L. Zhang, W. K. Pang, A. Du and Z. Guo, *Adv. Mater.*, 2021, **33**, 2006313.
46 Y. Wang, T. Wang, D. Dong, J. Xie, Y. Guan, Y. Huang, J. Fan and Y.-C. Lu, *Matter*, 2022, **5**, 162–179.
47 M. G. Giorgini, K. Futamatagawa, H. Torii, M. Musso and S. Cerini, *J. Phys. Chem. Lett.*, 2015, **6**, 3296–3302.
48 S. Di, X. Nie, G. Ma, W. Yuan, Y. Wang, Y. Liu, S. Shen and N. Zhang, *Energy Storage Mater.*, 2021, **43**, 375–382.
49 L. Cao, D. Li, T. Deng, Q. Li and C. Wang, *Angew. Chem., Int. Ed.*, 2020, **59**, 19292–19296.
50 J. Shi, T. Sun, J. Bao, S. Zheng, H. Du, L. Li, X. Yuan, T. Ma and Z. Tao, *Adv. Funct. Mater.*, 2021, **31**, 2102035.